



# Heterogeneous integration of a high-speed lithium niobate modulator on silicon nitride using micro-transfer printing

Cite as: APL Photon. 8, 086102 (2023); doi: 10.1063/5.0150878

Submitted: 16 March 2023 • Accepted: 11 July 2023 •

Published Online: 1 August 2023



View Online



Export Citation



CrossMark

T. Vanackere,<sup>1,2,a)</sup> T. Vandekerckhove,<sup>1,2</sup> L. Bogaert,<sup>1</sup> M. Billet,<sup>1,2</sup> S. Poelman,<sup>1</sup> S. Cuyvers,<sup>1</sup>   
J. Van Kerrebrouck,<sup>3</sup> A. Moerman,<sup>3</sup> O. Caytan,<sup>3</sup> N. Singh,<sup>3</sup> S. Lemey,<sup>3</sup> G. Torfs,<sup>3</sup> P. Ossieur,<sup>3</sup>   
C. Roelkens,<sup>1</sup> S. Clemmen,<sup>1,2,4</sup> and B. Kuyken<sup>1</sup>

## AFFILIATIONS

<sup>1</sup> Department of Information Technology (INTEC), Photonics Research Group, Ghent University–imec, 9052 Ghent, Belgium

<sup>2</sup> OPERA-Photonique CP 194/5, Université Libre de Bruxelles (ULB), 1050 Bruxelles, Belgium

<sup>3</sup> Department of Information Technology (INTEC), IDLab, Ghent University–imec, 9052 Ghent, Belgium

<sup>4</sup> Laboratoire d'Information Quantique, Université Libre de Bruxelles, 1050 Bruxelles, Belgium

<sup>a)</sup> Author to whom correspondence should be addressed: [Tom.Vanackere@ugent.be](mailto:Tom.Vanackere@ugent.be)

## ABSTRACT

Integrated photonic systems require fast modulators to keep up with demanding operation speeds and increasing data rates. The silicon nitride integrated photonic platform is of particular interest for applications such as datacom, light detection and ranging (LIDAR), quantum photonics, and computing owing to its low losses and CMOS compatibility. Yet, this platform inherently lacks high-speed modulators. Heterogeneous integration of lithium niobate on silicon nitride waveguides can address this drawback with its strong Pockels effect. We demonstrate the first high-speed lithium niobate modulator heterogeneously integrated on silicon nitride using micro-transfer printing. The device is 2 mm long with a half-wave voltage  $V_{\pi}$  of 14.8 V. The insertion loss and extinction ratio are 3.3 and 39 dB, respectively. Operation beyond 50 GHz has been demonstrated with the generation of open eye diagrams up to 70 Gb/s. This proof-of-principle demonstration opens up possibilities for more scalable fabrication of these trusted and performant devices.

© 2023 Author(s). All article content, except where otherwise noted, is licensed under a Creative Commons Attribution (CC BY) license (<http://creativecommons.org/licenses/by/4.0/>). <https://doi.org/10.1063/5.0150878>

## I. INTRODUCTION

Photonic systems are becoming faster and more complex as the technology evolves, and people are looking at a broader range of applications, from datacom, telecom,<sup>1</sup> and light detection and ranging (LIDAR)<sup>2</sup> over sensors<sup>3</sup> and medical devices<sup>4</sup> to optical neural networks<sup>5</sup> and on-chip (quantum) computing.<sup>6</sup> As we move toward integrating these elaborate systems into a chip, the requirement to densely co-integrate a very diverse set of functionalities increases. While most single functions have an integrated photonic platform that can perform them adequately, there is no integrated platform available that can perform all tasks optimally. Hence, in order to create more performant devices that can be used in complex integrated systems, people are looking at ways to combine different platforms to take advantage of each platform's strengths.

III–V platforms such as indium phosphide and gallium arsenide are great when it comes to providing efficient gain<sup>7,8</sup> and detection.<sup>9,10</sup>  $\chi^{(2)}$  nonlinear materials such as lithium niobate (LN), lead zirconate titanate, and gallium phosphide can be used for high speed modulation<sup>11,12</sup> and efficient frequency conversion.<sup>13–15</sup> When it comes to scaling and co-integration with electronics, the silicon (Si) and silicon nitride (SiN) photonics platforms take advantage of the mature CMOS technology developed for electronics.<sup>16</sup>

From these last two, the SiN integrated photonic platform, in particular, is a popular choice since it offers several distinct advantages over silicon-on-insulator. These benefits include a broader transparency window spanning into the visible,<sup>17</sup> a lower thermo-optic coefficient,<sup>18</sup> and significantly lower linear and nonlinear propagation losses when working at a wavelength of 1550 nm<sup>19</sup>

compared to silicon-on-insulator. It is, however, a purely passive platform that lacks light sources and efficient high-speed detectors and modulators. In order to achieve faster modulation on both the Si and SiN platforms, heterogeneous integration with III-V,<sup>20,21</sup> graphene,<sup>22–24</sup> germanium,<sup>25</sup> organics,<sup>26,27</sup> lead zirconate titanate (PZT),<sup>12</sup> barium titanate,<sup>28,29</sup> and LN has been heavily explored.

Lithium niobate (LN) has historically been a work horse for optical modulation functionalities in datacom links. This is due to its high Pockels coefficient and low losses. The arrival of thin film lithium niobate (TFLN) with sub-micron thickness was instrumental in the further development of these modulators, bringing them one step closer to the reduced form factor and increased performance that integrated devices offer. Progress on its etching<sup>30,31</sup> allowed for many impressive realizations, such as integrated modulators reaching bandwidths over 100 GHz with CMOS compatible driving voltages.<sup>11,32–35</sup> Additionally, these TFLN structures have been used to exploit several nonlinear phenomena.<sup>36,37</sup>

TFLN devices have also been heterogeneously integrated through wafer bonding,<sup>38,39</sup> but these devices often still require further processing after the bonding process. Micro-transfer printing ( $\mu$ TP) is a heterogeneous integration method that allows for the integration of devices<sup>40–42</sup> and thin films<sup>43,44</sup> at the back-end of the fabrication process. It is beneficial that this be done as late in the process flow as possible since some of the fabrication steps and materials are incompatible with CMOS fabrication standards. This is particularly the case with lithium niobate due to the risks of lithium contamination.

Transfer printing enables the completion of all of the lithium niobate device fabrication processes separately from the nitride fabrication, requiring no further processing after the printing other than a simple metallization step.<sup>45,46</sup> If needed, even this metallization step can be omitted by depositing it on the coupon before printing. Furthermore, the prefabrication of the transfer printing

coupons allows for the efficient use of the LN material and the close integration of different materials from different source wafers onto the same integrated chip system.

In this paper, we demonstrate the first high-speed lithium niobate modulator heterogeneously integrated on silicon nitride using micro-transfer printing. The device is 2 mm long, has an insertion loss of 3.3 dB, and a half-wave voltage ( $V_{\pi}$ ) of 14.8 V. We were able to measure a 3 dB bandwidth of over 50 GHz, which allowed us to generate 70 Gb/s non-return-to-zero (NRZ) data.

## II. DESIGN AND SIMULATIONS

The modulator consists of two phase modulator sections combined with two  $1 \times 2$  multimode interferometers (MMI) to form a Mach-Zehnder modulator (MZM) in a push-pull configuration. A schematic image is shown in Fig. 1(a). Grating couplers are used to couple the light in and out of the SiN waveguide. The phase modulators use a hybrid waveguide comprising a 300 nm thick SiN strip waveguide with a 300 nm slab of x-cut LN on top. The fundamental TE-polarized mode at a wavelength of 1550 nm is guided by the  $1 \mu\text{m}$  wide SiN waveguide; the mode has a large overlap with the LN slab as shown in the inset in Fig. 1(a). Electrodes consisting of 15 nm titanium (Ti) and  $1 \mu\text{m}$  gold (Au) are placed on both sides of each waveguide. Through co-simulation of both electrical and optical fields in COMSOL Multiphysics®, the SiN waveguide width and the gap between the electrodes are chosen to minimize the half-wave voltage-length product ( $V_{\pi}L$ ) while not introducing additional losses due to absorption in the metal. This leads to a SiN waveguide width of  $1 \mu\text{m}$  and an electrode gap of  $6 \mu\text{m}$ , resulting in a  $V_{\pi}L$  of 6.0 V cm for a single phase section (3.0 V cm for the device in push-pull configuration).

In order to reduce the index mismatch at the transition from the nitride waveguide to the hybrid LN-on-SiN waveguide, the

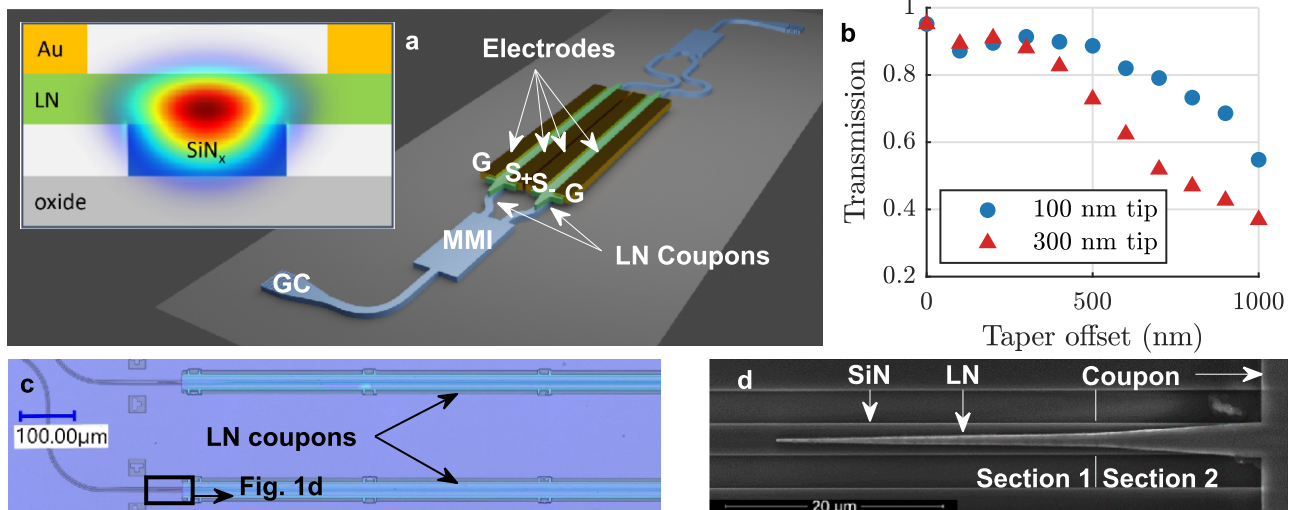


**FIG. 1.** (a) Schematic image of the complete device. (inset) Overview of the hybrid LN-on-SiN mode profile. Both the SiN and the LN layers are 300 nm thick. The SiN waveguide is  $1 \mu\text{m}$  wide. (b) Simulation results of the  $45 \mu\text{m}$  long bilinear taper as a function of the taper tip width and alignment offset. (c) Microscope image of the printed LN coupons on SiN waveguides. (d) SEM image of the LN taper.

coupons are fabricated with adiabatic tapers on both ends; see Fig. 1(d). These tapers are optimized in Lumerical simulations to be as short as possible to facilitate the transfer while still being robust to at most  $0.5\ \mu\text{m}$  of misalignment, which is the  $3\sigma$  alignment accuracy of the transfer printing tool. The tapers consist of two linear sections to keep them short at a total length of  $45\ \mu\text{m}$ . In order to increase the transmission in case of misalignment, the nitride waveguide is also locally tapered to a  $3\ \mu\text{m}$  width at the transition sections. The simulated transmission of the tapers for different taper tip widths and misalignments is shown in Fig. 1(b). While a narrower taper tip would perform better, our fabrication methods limit how narrow we can make the tip, and we aim for a  $200\ \text{nm}$  width. Simulations tell us that increasing the length of the tapers does little to increase the transmission at larger misalignments since the reduced transmission is caused by the excitation of higher order modes and reflections at the facets. This is elaborated on in the supplementary material.

The MZM is designed with a Ground-Signal-Signal-Ground (GSSG) electrode configuration in the interest of matching it to a specific driver chip in the future. In order to achieve high-speed operation, these electrodes are also designed using CST Studio Suite<sup>®</sup> to have their differential mode impedance matched to  $100\ \Omega$  while providing a phase velocity close to the group velocity of the optical mode in order to achieve traveling wave behavior up to  $100\ \text{GHz}$ . The impedance matching is achieved by changing the electrode width and height, while the traveling wave behavior is ensured by optimizing the buried oxide thickness. The resulting values are an electrode width and height of  $35$  and  $1\ \mu\text{m}$ , respectively, and an oxide thickness of  $3.3\ \mu\text{m}$ . The electrodes are then fitted with a short fan-out taper to the contact pads with a pitch of  $125\ \mu\text{m}$ .

### III. FABRICATION

The x-cut LN source chip and the SiN target chip are fabricated separately but in parallel. The source chip is patterned to create rectangular coupons with a length of  $2\ \text{mm}$  and a width of  $30\ \mu\text{m}$ . The coupons include tapers on both sides and tethers to mechanically keep the coupon connected to the rest of the chip during release. This pattern is defined using e-beam lithography and first transferred to an amorphous silicon (a-Si) hard mask using reactive-ion etching (RIE). After patterning the hard mask, an Ar milling RIE recipe is used to transfer the pattern to the  $300\ \text{nm}$  thick LN layer. The hard mask is then removed, and the silicon oxide layer underneath the coupons is wet-etched away using hydrofluoric acid in order to release the coupon. At this point, the coupons are suspended but still attached to the rest of the chip through the tethers and are ready to be picked-up and printed.<sup>45</sup> The tethers include a hole, or “crack barrier,” in order to prevent the breaking tether from also breaking the entire coupon.<sup>47</sup> The optical structures on the nitride chip are also patterned using a combination of e-beam lithography and dry-etching.

Both chips are then loaded into the transfer printing tool, where a stamp is used to pick up the LN coupons. The stamp is a polydimethylsiloxane (PDMS) elastomer, which has a stronger adhesion when moving faster. Details about the printing process can be found in Refs. 40 and 48. This process is fast, can be done in parallel, and can be automated, making it suitable for mass fabrication. Contrary to wafer bonding, now that the LN is on the target chip, no additional etching step is required, avoiding compatibility issues. Moreover,

since the transfer printing process only transfers a piece of material, it is possible to closely integrate other heterogeneous materials on the same die. The result after printing is shown in Fig. 1(c). We printed 32 coupons, and 27 of them were successful; these also all had an alignment within  $0.5\ \mu\text{m}$  on all taper sections. Since then, the method has improved, and the results shown in Ref. 48 show a 100% yield for a series of 25 coupons. A scanning electron microscope (SEM) image of a printed taper is shown in Fig. 1(d). While the alignment is as expected, the etching process is not ideal, such that the resulting taper structure deviates from the design, with a tip width closer to  $300\ \text{nm}$  than the intended  $200\ \text{nm}$ . A final optical lithography step is used to define the electrodes. A simple metallization and lift-off process finish the chip. We noticed a slight misalignment of the electrodes after fabrication.

### IV. MEASUREMENTS AND RESULTS

The chip is first measured at low speeds in order to characterize the optical and electro-optical performance of the printed devices. Comparing a reference waveguide with and without printed coupons (both without electrodes) results in an excess transmission loss of the printed structure of  $2.7\ \text{dB}$ . The insertion loss of the MZM structures with printed coupons is  $0.6\ \text{dB}$  higher, giving a total of  $3.3\ \text{dB}$ . This additional loss is explained by a  $0.3\ \text{dB}$  excess loss per MMI, as measured in dedicated cascaded MMI test structures. The  $2.7\ \text{dB}$  insertion loss per coupon is worse than the ideal simulated value of  $0.25\ \text{dB}$ . This discrepancy is mainly a result of a wider taper tip, the printing misalignment, and, to a lesser extent, the side wall roughness. While the fabrication of these tapers limits their functionality, the result is still better than a sudden transition without a taper, which causes a  $1.8\ \text{dB}$  loss per transition.<sup>45</sup>

Figure 2(a) shows a wavelength sweep of the MZM transmission, which shows an extinction ratio of  $39\ \text{dB}$  near  $1550\ \text{nm}$ . The nitride chip was designed with an imbalanced Mach-Zehnder interferometer (MZI) design, resulting in a free spectral range of  $9.5\ \text{nm}$ . A voltage sweep at the quadrature point indicates a  $V_\pi$  of  $14.8\ \text{V}$ , as shown in Fig. 2(b). Considering the  $2\ \text{mm}$  length and push-pull functionality of the device, this is close to the  $6.0\ \text{V/cm}$  per phase modulator from the simulation or  $3.0\ \text{V/cm}$  for the MZM.

The electrodes are characterized up to  $67\ \text{GHz}$  using a vector network analyzer (VNA, Keysight N5247A PNA-X) to perform an S-parameter measurement. A calibration substrate is used to calibrate the contact pads. The electrical characteristics of the differential mode are shown in Fig. 3. The characteristic impedance of the transmission line is close to the desired  $100\ \Omega$ . Furthermore, Fig. 3(a) visualizes the electrical losses of the modulator, resulting in around  $2\ \text{dB/mm}$  attenuation at frequencies over  $10\ \text{GHz}$ . From simulations and tests with similar electrodes on SiN and glass, this largely seems to be caused by ohmic losses in the substrate and could, therefore, be avoided using a high-resistivity silicon substrate. More details on this can be found in the supplementary material. The effective index of the mode is also close to the optical group index, as shown in Fig. 3(b).

Subsequently, the electro-optical performance is characterized by high speeds in both the frequency and time domains. Figure 4(a) shows a schematic representation of the setup used for the frequency domain measurements. A Santec (Santec TSL-510) laser is used as a CW-source at  $1550\ \text{nm}$ . The light is sent through a polarization

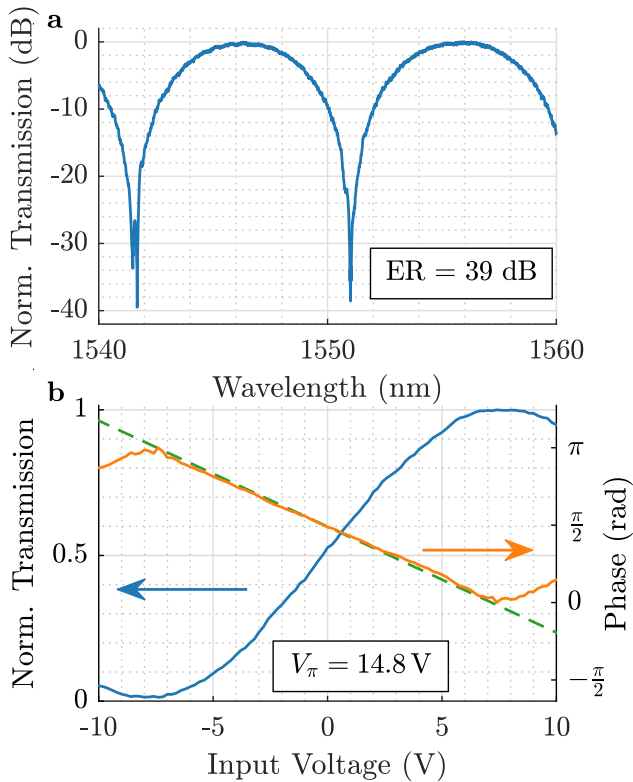


**FIG. 2.** Low frequency measurement results. (a) Normalized wavelength sweep of the MZI structure, the free spectral range is 9.5 nm and the extinction ratio is 39 dB. (b) Output power as a function of the applied voltage (blue line). Extracted phase change depending on the applied voltage (orange line), fitted linear phase change resulting in a  $V_{\pi}$  of 14.8 V (green striped line).

controller before being coupled to the chip using a grating coupler. The output light is split 99:1, where one percent of the light goes to a Newport power meter to continuously monitor the transmission during the measurement. The rest of the light is sent to an erbium doped fiber amplifier (EDFA, Keopsys CEFA-C-HG), followed by an Optical Spectral Filter (OTF) set to a 2 nm optical bandwidth (Santec OTF-350). The light is then detected using a 70 GHz uni-traveling-carrier (UTC) photodiode (XPDV3120R). The transmission line is probed on one side by the VNA and terminated on the other side by using probes connected to 50  $\Omega$  terminations. For the electro-optical frequency domain measurement, we start by calibrating the cables from the VNA to the modulator inputs and the cable from the photodiode output to the VNA. Afterward, the probe and diode characteristics themselves are subtracted in post-processing. The resulting measurement is shown in Fig. 4(b). The device has a 3 dB bandwidth exceeding 50 GHz, which is limited by the measurement equipment. Due to the high  $V_{\pi}$ , the signal quickly hits the noise floor of the VNA. There is a small feature around 11.8 GHz that is due to a piezo-electrical resonance that is explained in more detail in the supplementary material.

The setup used to perform the time domain measurements is shown schematically in Fig. 5(a). The setup is similar to the time

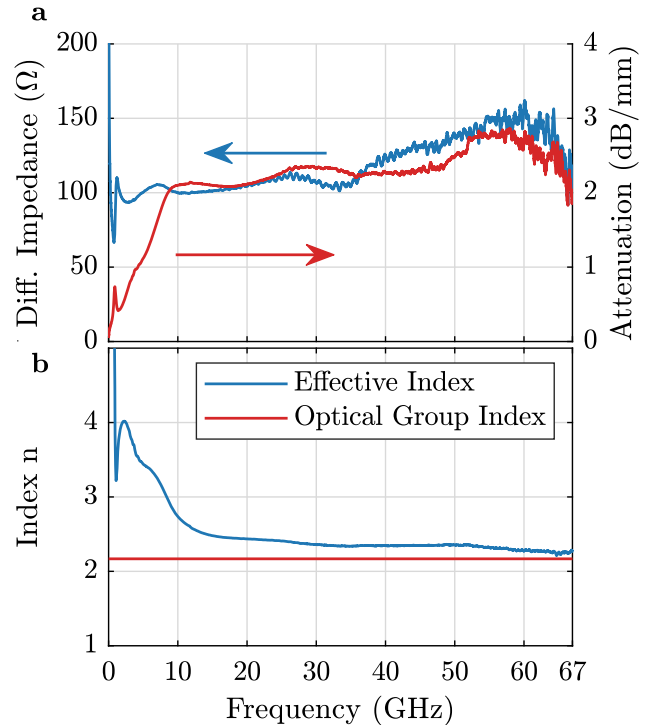


**FIG. 3.** High speed electrical characteristics. [(a) left] The characteristic impedance of the differential transmission line as a function of the modulation frequency. [(a) right] Electrical attenuation as a function of the modulation frequency. (b) Effective electrical index as a function of the modulation frequency; the red line is the target optical group index.

domain setup from the optical point of view but relies on a differential signal generated by an AWG (Keysight M8196A), which is first amplified before it enters the modulator chip via the RF probe. In addition, the signal coming from the diode is now amplified before being sent to the sampling scope (Keysight N1000A DCA-X). These three forms of amplification (electrical before modulation and after detection, and optical through an EDFA) are needed to generate a visible signal on the sampling scope. Using a laser output power of 20 mW, we are able to generate up to 70 Gb/s NRZ using raised cosine signals with a bit error rate (BER) below KP4-forward error correction (FEC) after equalization of the high-speed modulator input (AWG + cables + electrical pre-amplification). Figure 5(b) shows the different error rates as a function of modulation speed. The electrical back-to-back measurement and eyes of the 56 and 70 Gb/s points are also included. Using the low speed measurements, we estimate that the 4.4 V peak-to-peak input signal at 56 Gb/s will result in an approximate extinction ratio of 3.7 dB between the 1 and 0 levels at the output of the chip. The measurement could be improved by using better grating couplers or horizontal coupling. The EDFA is needed in these measurements due to a loss of around 18 dB from both gratings combined, on top of the insertion loss of the device. The noise from unmodulated light that has gone through the EDFA increases from 24 mV on the sampling scope (PD thermal noise) to 64 mV (PD thermal noise + EDFA noise), severely reducing

25 August 2023 09:05:20

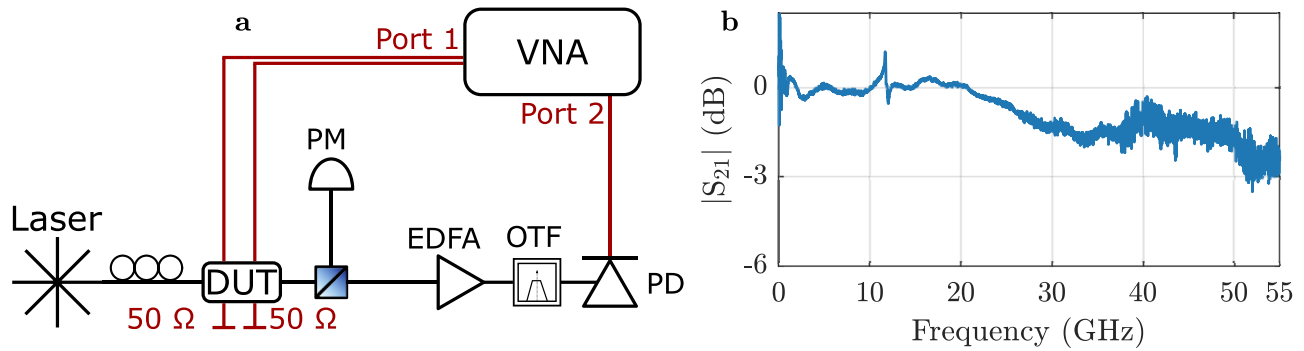


**FIG. 4.** (a) Schematic overview of the measurement setup used to perform the frequency domain measurements. (PM = Power Meter, EDFA = Erbium Doped Fiber Amplifier, OTF = Optical Tunable Filter, PD = Photodiode, VNA = Vector Network Analyzer, DUT = Device Under Test) (b) Measured  $|S_{21}|$  as a function of the modulation frequency, obtained by using the setup in (a). The measurement hits the noise floor around 55 GHz.

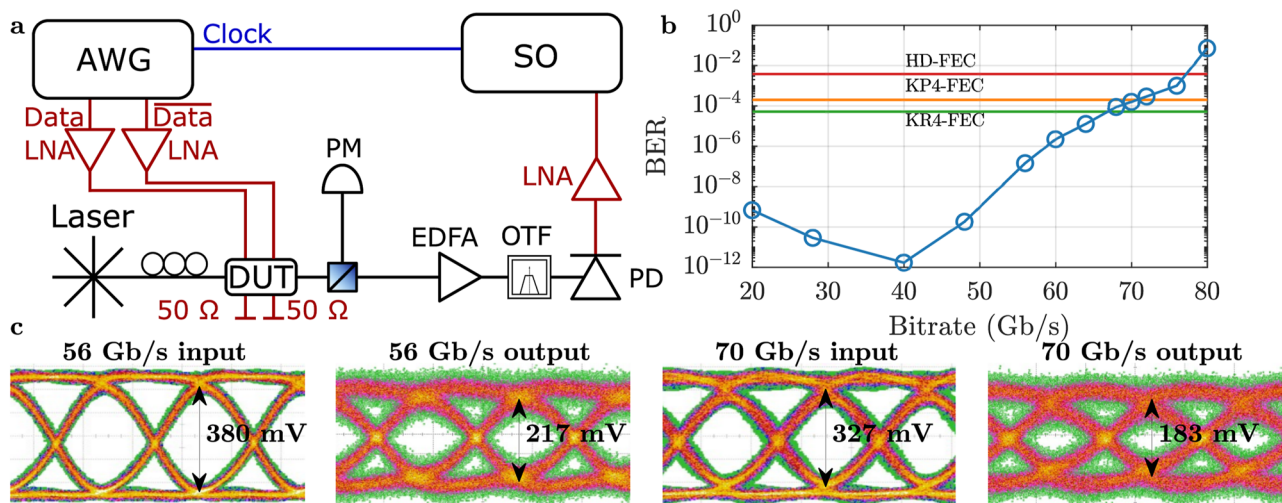


**FIG. 5.** (a) Schematic overview of the measurement setup used to perform the time domain measurements. (AWG = Arbitrary Waveform Generator, SO = Sampling Oscilloscope, LNA = Low Noise Amplifier, PM = Power Meter, EDFA = Erbium Doped Fiber Amplifier, OTF = Optical Tunable Filter, PD = Photodiode, and DUT = Device Under Test) (b) Bit error rate measured by using the setup in (a) as a function of the bitrate. KR4-FEC, KP4-FEC, and HD-FEC are included as references. (c) Electrical back-to-back and resulting electro-optically generated eye diagrams for 56 and 70 Gb/s. The electrical back-to-back eyes were attenuated by 20 dB before entering the sampling oscilloscope. The Q factors of these eyes are from left to right: 12.18, 5.13, 6.85, and 3.60.

the quality of the eye diagrams. Furthermore, the electrical amplifiers, AWG, and sampling scope are also reaching their speed limit at the highest bit rates, as seen from the reduced input eye quality at 70 Gb/s in Fig. 5(c).

## V. CONCLUSIONS AND FUTURE OUTLOOK

In this paper, we demonstrate the first high-speed modulator using hybrid LN-on-SiN waveguides fabricated with micro-transfer printing. The device shows an insertion loss of 3.3 dB, an extinction ratio of 39 dB, and a  $V_{\pi}$  of 14.8 V. Operation up to at least 50 GHz has been demonstrated with the generation of eye diagrams up to 70 Gb/s. The most obvious way of improving the device is by increasing the length of the device, and we are confident coupons

up to at least 1 cm can be printed, which would strongly reduce the  $V_{\pi}$ . At that point, the ohmic losses are also best addressed by using a high-resistivity substrate. Furthermore, higher quality fabrication of the grating couplers, MMIs, and electrodes can improve the device and make it easier to characterize at speeds larger than 55 GHz. Additionally, adding heaters for thermal tuning of the bias point and using a symmetric MZI design would decouple the working point from the wavelength choice. Finally, state-of-the-art etching of the LN in order to create better tapers and even define a rib waveguide in the LN coupon, to increase the confinement in the LN, would increase the performance of the device by reducing the  $V_{\pi}L$  in simulation from 6.0 V cm in our hybrid LN-on-SiN waveguides to values similar to those achieved in pure LN rib waveguides.

## SUPPLEMENTARY MATERIAL

The supplementary material contains three sections. The first section concerns a piezo-electric resonance that clarifies the kink around 12 GHz in Fig. 4(b). The second section shows some more measurements and a simulation to explain the unexpected behavior of the RF attenuation from Fig. 3(c). The third goes a bit deeper into the taper design, taking into account the transfer printing alignment accuracy.

## ACKNOWLEDGMENTS

Tom Vanackere, Tom Vandekerckhove, and Stijn Cuyvers are Ph.D. fellows of the Research Foundation Flanders (FWO) under respective grant numbers 11F5320N, 11H6721N and 11F8120N. Stéphane Clemmen is a research associate of the Fonds de la Recherche Scientifique–FNRS in the context of Grant No. MIS F.4506.20. We also thank the European Research Council (ERC) for the funding in the context of the ELECTRIC project.

## AUTHOR DECLARATIONS

### Conflict of Interest

The authors have no conflicts to disclose.

## Author Contributions

**T. Vanackere:** Conceptualization (lead); Data curation (lead); Formal analysis (lead); Funding acquisition (supporting); Investigation (lead); Methodology (lead); Software (lead); Visualization (lead); Writing – original draft (lead); Writing – review & editing (lead). **T. Vandekerckhove:** Investigation (supporting); Validation (equal); Writing – review & editing (supporting). **L. Bogaert:** Formal analysis (supporting); Investigation (supporting); Writing – review & editing (supporting). **M. Billet:** Conceptualization (supporting); Writing – review & editing (supporting). **S. Poelman:** Investigation (supporting); Methodology (supporting); Writing – review & editing (supporting). **S. Cuyvers:** Visualization (supporting); Writing – review & editing (supporting). **J. Van Kerrebrouck:** Formal analysis (supporting); Methodology (supporting); Writing – review & editing (supporting). **A. Moerman:** Methodology (supporting); Software (supporting); Validation (equal); Writing – review & editing (supporting). **O. Caytan:** Methodology (supporting); Software (supporting); Validation (equal); Writing – review & editing (supporting). **N. Singh:** Methodology (supporting); Software (supporting); Validation (equal); Writing – review & editing (supporting). **S. Lemey:** Funding acquisition (supporting); Writing – review & editing (supporting). **G. Torfs:** Funding acquisition (supporting); Writing – review & editing (supporting). **P. Ossieur:** Funding acquisition (supporting); Writing – review & editing (supporting). **G. Roelkens:** Resources (equal); Writing – review & editing (supporting). **S. Clemmen:** Conceptualization (supporting); Funding acquisition (equal); Resources (equal); Supervision (equal); Writing – review & editing (supporting). **B. Kuyken:** Conceptualization (supporting); Funding acquisition (equal); Project administration

(lead); Resources (equal); Supervision (equal); Writing – review & editing (supporting).

## DATA AVAILABILITY

The data that support the findings of this study are available from the corresponding author upon reasonable request.

## REFERENCES

- A. H. Atabaki, S. Moazeni, F. Pavanello, H. Gevorgyan, J. Notaros, L. Alloatti, M. T. Wade, C. Sun, S. A. Kruger, H. Meng *et al.*, “Integrating photonics with silicon nanoelectronics for the next generation of systems on a chip,” *Nature* **556**, 349–354 (2018).
- C. V. Poulton, M. J. Byrd, P. Russo, B. Moss, O. Shatrovov, M. Khandaker, and M. R. Watts, “Coherent LiDAR with an 8,192-element optical phased array and driving laser,” *IEEE J. Sel. Top. Quantum Electron.* **28**, 6100508 (2022).
- W. J. Westerveld, M. Mahmud-Ul-Hasan, R. Shnaiderman, V. Ntziachristos, X. Rottenberg, S. Severi, and V. Rochus, “Sensitive, small, broadband and scalable optomechanical ultrasound sensor in silicon photonics,” *Nat. Photonics* **15**, 341–345 (2021).
- P. T. Lin, H.-Y. G. Lin, Z. Han, T. Jin, R. Millender, L. C. Kimerling, and A. Agarwal, “Label-free glucose sensing using chip-scale mid-infrared integrated photonics,” *Adv. Opt. Mater.* **4**, 1755–1759 (2016).
- G. Mourgas-Alexandris, M. Moralis-Pegios, A. Tsakyridis, S. Simos, G. Dabos, A. Totovic, N. Passalis, M. Kirtas, T. Rutirawut, F. Y. Gardes, A. Tefas, and N. Pleros, “Noise-resilient and high-speed deep learning with coherent silicon photonics,” *Nat. Commun.* **13**, 5572 (2022).
- J. Wang, F. Sciarrino, A. Laing, and M. G. Thompson, “Integrated photonic quantum technologies,” *Nat. Photonics* **14**, 273–284 (2020).
- W. K. Ng, Y. Han, K. M. Lau, and K. S. Wong, “Broadband telecom emission from InP/InGaAs nano-ridge lasers on silicon-on-insulator substrate,” *OSA Continuum* **2**, 3037–3043 (2019).
- B. Haq, S. Kumari, K. Van Gasse, J. Zhang, A. Gocalinska, E. Pelucchi, B. Corbett, and G. Roelkens, “Micro-transfer-printed III-V-on-silicon C-band semiconductor optical amplifiers,” *Laser Photonics Rev.* **14**, 1900364 (2020).
- F. Xiao, Q. Han, H. Ye, S. Wang, and F. Xiao, “InP-based high-speed monolithic PIN photodetector integrated with an MQW semiconductor optical amplifier,” *Jpn. J. Appl. Phys.* **61**, 012005 (2022).
- M. Smit, K. Williams, and J. van der Tol, “Past, present, and future of InP-based photonic integration,” *APL Photonics* **4**, 050901 (2019).
- M. Zhang *et al.*, “Integrated lithium niobate electro-optic modulators: When performance meets scalability,” *Optica* **8**, 652–667 (2021).
- K. Alexander, J. P. George, J. Verbist, K. Neyts, B. Kuyken, D. Van Thourhout, and J. Beekman, “Nanophotonic Pockels modulators on a silicon nitride platform,” *Nat. Commun.* **9**, 3444 (2018).
- G. F. Feutmba, A. Hermans, J. P. George, H. Rijckaert, I. Ansari, D. Van Thourhout, and J. Beekman, “Reversible and tunable second-order nonlinear optical susceptibility in PZT thin films for integrated optics,” *Adv. Opt. Mater.* **9**, 2100149 (2021).
- A. P. Anthur, H. Zhang, Y. Akimov, J. R. Rong Ong, D. Kalashnikov, A. I. Kuznetsov, and L. Krivitsky, “Second harmonic generation in gallium phosphide nano-waveguides,” *Opt. Express* **29**, 10307–10320 (2021).
- D. J. Wilson, K. Schneider, S. Hönl, M. Anderson, Y. Baumgartner, L. Czornomaz, T. J. Kippenberg, and P. Seidler, “Integrated gallium phosphide nonlinear photonics,” *Nat. Photonics* **14**, 57–62 (2020).
- W. Bogaerts, M. Fiers, and P. Dumon, “Design challenges in silicon photonics,” *IEEE J. Sel. Top. Quantum Electron.* **20**, 8202008 (2013).
- A. Rahim, E. Ryckeboer, A. Z. Subramanian, S. Clemmen, B. Kuyken, A. Dhakal, A. Raza, A. Hermans, M. Muneeb, S. Dhoore *et al.*, “Expanding the silicon photonics portfolio with silicon nitride photonic integrated circuits,” *J. Lightwave Technol.* **35**, 639–649 (2017).

- <sup>18</sup>A. Arbabi and L. L. Goddard, "Measurements of the refractive indices and thermo-optic coefficients of  $\text{Si}_3\text{N}_4$  and  $\text{SiO}_x$  using microring resonances," *Opt. Lett.* **38**, 3878–3881 (2013).
- <sup>19</sup>D. J. Moss, R. Morandotti, A. L. Gaeta, and M. Lipson, "New CMOS-compatible platforms based on silicon nitride and Hydex for nonlinear optics," *Nat. Photonics* **7**, 597–607 (2013).
- <sup>20</sup>J.-H. Han, F. Boeuf, J. Fujikata, S. Takahashi, S. Takagi, and M. Takenaka, "Efficient low-loss InGaAsP/Si hybrid MOS optical modulator," *Nat. Photonics* **11**, 486–490 (2017).
- <sup>21</sup>T. Hiraki, T. Aihara, K. Hasebe, K. Takeda, T. Fujii, T. Kakitsuka, T. Tsuchizawa, H. Fukuda, and S. Matsuo, "Heterogeneously integrated III–V/Si MOS capacitor Mach–Zehnder modulator," *Nat. Photonics* **11**, 482–485 (2017).
- <sup>22</sup>C. T. Phare, Y.-H. Daniel Lee, J. Cardenas, and M. Lipson, "Graphene electro-optic modulator with 30 GHz bandwidth," *Nat. Photonics* **9**, 511–514 (2015).
- <sup>23</sup>V. Sorianoello, M. Midrio, G. Contestabile, I. Asselberghs, J. Van Campenhout, C. Huyghebaert, I. Goykhman, A. K. Ott, A. C. Ferrari, and M. Romagnoli, "Graphene–silicon phase modulators with gigahertz bandwidth," *Nat. Photonics* **12**, 40–44 (2018).
- <sup>24</sup>H. Shu, Z. Su, L. Huang, Z. Wu, X. Wang, Z. Zhang, and Z. Zhou, "Significantly high modulation efficiency of compact graphene modulator based on silicon waveguide," *Sci. Rep.* **8**, 991 (2018).
- <sup>25</sup>S. A. Srinivasan, M. Pantouvakis, S. Gupta, H. T. Chen, P. Verheyen, G. Lepage, G. Roelkens, K. Saraswat, D. Thourhout, P. Absil, and J. V. Campenhout, "56 Gb/s germanium waveguide electro-absorption modulator," *J. Lightwave Technol.* **34**, 419–424 (2016).
- <sup>26</sup>C. Koos, W. Freude, D. Kohler, J. Milvich, C. Kieninger, and H. Zwickel, "Silicon organic hybrid (SOH) and silicon-nitride-organic hybrid (SiNOH) integration: From electro-optic modulators to visible-wavelength lasers," *Proc. SPIE* **PC12004**, PC120040B (2022).
- <sup>27</sup>L. Alloatti, R. Palmer, S. Diebold, K. P. Pahl, B. Chen, R. Dinu, M. Fournier, J.-M. Fedeli, T. Zwick, W. Freude *et al.*, "100 GHz silicon–organic hybrid modulator," *Light: Sci. Appl.* **3**, e173 (2014).
- <sup>28</sup>F. Eltes, M. Kroh, D. Caimi, C. Mai, Y. Popoff, G. Winzer, D. Petousi, S. Lischke, J. E. Ortmann, L. Czornomaz *et al.*, "A novel 25 Gbps electro-optic Pockels modulator integrated on an advanced Si photonic platform," in *2017 IEEE International Electron Devices Meeting (IEDM)* (IEEE, 2017), pp. 24–25.
- <sup>29</sup>F. Eltes, C. Mai, D. Caimi, M. Kroh, Y. Popoff, G. Winzer, D. Petousi, S. Lischke, J. E. Ortmann, L. Czornomaz, L. Zimmermann, J. Fompeyrine, and S. Abel, "A  $\text{BaTiO}_3$ -based electro-optic Pockels modulator monolithically integrated on an advanced silicon photonics platform," *J. Lightwave Technol.* **37**, 1456–1462 (2019).
- <sup>30</sup>C. Wang, M. J. Burek, Z. Lin, H. A. Atikian, V. Venkataraman, I.-C. Huang, P. Stark, and M. Lončar, "Integrated high quality factor lithium niobate microdisk resonators," *Opt. Express* **22**, 30924–30933 (2014).
- <sup>31</sup>M. Zhang, C. Wang, R. Cheng, A. Shams-Ansari, and M. Lončar, "Monolithic ultra-high-Q lithium niobate microring resonator," *Optica* **4**, 1536–1537 (2017).
- <sup>32</sup>C. Wang, M. Zhang, X. Chen, M. Bertrand, A. Shams-Ansari, S. Chandrasekhar, P. Winzer, and M. Lončar, "Integrated lithium niobate electro-optic modulators operating at CMOS-compatible voltages," *Nature* **562**, 101–104 (2018).
- <sup>33</sup>M. Xu, M. He, H. Zhang, J. Jian, Y. Pan, X. Liu, L. Chen, X. Meng, H. Chen, Z. Li *et al.*, "High-performance coherent optical modulators based on thin-film lithium niobate platform," *Nat. Commun.* **11**, 3911 (2020).
- <sup>34</sup>C. Wang, M. Zhang, X. Chen, M. Bertrand, A. Shams-Ansari, S. Chandrasekhar, P. Winzer, and M. Lončar, "100-GHz low voltage integrated lithium niobate modulators," in *2018 Conference on Lasers and Electro-Optics (CLEO)* (IEEE, 2018), pp. 1–2.
- <sup>35</sup>M. Xu, Y. Zhu, F. Pittalà, J. Tang, M. He, W. C. Ng, J. Wang, Z. Ruan, X. Tang, M. Kuschnerov, L. Liu, S. Yu, B. Zheng, and X. Cai, "Dual-polarization thin-film lithium niobate in-phase quadrature modulators for terabit-per-second transmission," *Optica* **9**, 61–62 (2022).
- <sup>36</sup>C. Wang, C. Langrock, A. Marandi, M. Jankowski, M. Zhang, B. Desiatov, M. M. Fejer, and M. Lončar, "Ultrahigh-efficiency wavelength conversion in nanophotonic periodically poled lithium niobate waveguides," *Optica* **5**, 1438–1441 (2018).
- <sup>37</sup>A. Boes, L. Chang, C. Langrock, M. Yu, M. Zhang, Q. Lin, M. Lončar, M. Fejer, J. Bowers, and A. Mitchell, "Lithium niobate photonics: Unlocking the electromagnetic spectrum," *Science* **379**, eabj4396 (2023).
- <sup>38</sup>M. He, M. Xu, Y. Ren, J. Jian, Z. Ruan, Y. Xu, S. Gao, S. Sun, X. Wen, L. Zhou, L. Liu, C. Guo, H. Chen, S. Yu, L. Liu, and X. Cai, "High-performance hybrid silicon and lithium niobate Mach–Zehnder modulators for 100 Gbit  $\text{s}^{-1}$  and beyond," *Nat. Photonics* **13**, 359–364 (2019).
- <sup>39</sup>P. O. Weigel, J. Zhao, K. Fang, H. Al-Rubaye, D. Trotter, D. Hood, J. Mudrick, C. Dallo, A. T. Pomerene, A. L. Starbuck, C. T. DeRose, A. L. Lentine, G. Rebeiz, and S. Mookherjee, "Bonded thin film lithium niobate modulator on a silicon photonics platform exceeding 100 GHz 3-dB electrical modulation bandwidth," *Opt. Express* **26**, 23728–23739 (2018).
- <sup>40</sup>G. Roelkens, J. Zhang, L. Bogaert, M. Billet, D. Wang, B. Pan, C. J. Kruckel, E. Soltanian, D. Maes, T. Vanackere, T. Vandekerckhove, S. Cuyvers, J. De Witte, I. L. Lufungula, X. Guo, H. Li, S. Qin, G. Muliuk, S. Uvin, B. Haq, C. Op de Beeck, J. Goyvaerts, G. Lepage, P. Verheyen, J. Van Campenhout, G. Morthier, B. Kuyken, D. Van Thourhout, and R. Baets, "Micro-transfer printing for heterogeneous Si photonic integrated circuits," *IEEE J. Sel. Top. Quantum Electron.* **29**, 8200414 (2022).
- <sup>41</sup>J. Justice, C. Bower, M. Meitl, M. B. Mooney, M. A. Gubbins, and B. Corbett, "Wafer-scale integration of group III–V lasers on silicon using transfer printing of epitaxial layers," *Nat. Photonics* **6**, 610–614 (2012).
- <sup>42</sup>B. Corbett, R. Loi, W. Zhou, D. Liu, and Z. Ma, "Transfer print techniques for heterogeneous integration of photonic components," *Prog. Quantum Electron.* **52**, 1–17 (2017).
- <sup>43</sup>M. Billet, L. Reis, Y. Léger, C. Cornet, F. Raineri, I. Sagnes, K. Pantzas, G. Beaudoin, G. Roelkens, F. Leo, and B. Kuyken, "Gallium phosphide-on-insulator integrated photonic structures fabricated using micro-transfer printing," *Opt. Mater. Express* **12**, 3731–3737 (2022).
- <sup>44</sup>J. McPhillimy, B. Guilhabert, C. Klitis, M. D. Dawson, M. Sorel, and M. J. Strain, "High accuracy transfer printing of single-mode membrane silicon photonic devices," *Opt. Express* **26**, 16679–16688 (2018).
- <sup>45</sup>T. Vanackere, M. Billet, C. Op de Beeck, S. Poelman, G. Roelkens, S. Clemmen, and B. Kuyken, "Micro-transfer printing of lithium niobate on silicon nitride," in *2020 European Conference on Optical Communications (ECOC)* (IEEE, 2020), pp. 1–4.
- <sup>46</sup>Z. Li, J. A. Smith, M. Scullion, N. K. Wessling, L. J. McKnight, M. D. Dawson, and M. J. Strain, "Photonic integration of lithium niobate micro-ring resonators onto silicon nitride waveguide chips by transfer-printing," *Opt. Mater. Express* **12**, 4375–4383 (2022).
- <sup>47</sup>S. Cuyvers, T. Vanackere, T. Vandekerckhove, S. Poelman, C. Op de Beeck, J. De Witte, A. Hermans, K. Van Gasse, N. Picqué, D. Van Thourhout, G. Roelkens, S. Clemmen, and B. Kuyken, "High-yield heterogeneous integration of silicon and lithium niobate thin films," in *2022 Conference on Lasers and Electro-Optics (CLEO)* (IEEE, 2022), pp. 1–2.
- <sup>48</sup>T. Vandekerckhove, T. Vanackere, J. D. De Witte, S. Cuyvers, L. Reis, M. Billet, G. Roelkens, S. Clemmen, and B. Kuyken, "Reliable micro-transfer printing method for heterogeneous integration of lithium niobate and semiconductor thin films," *Opt. Mater. Express* **13**, 1984–1993 (2023).